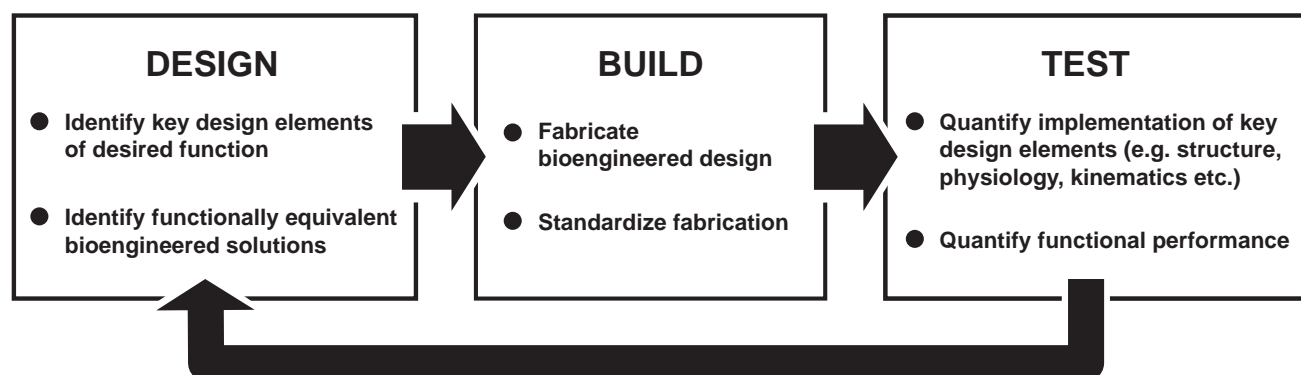
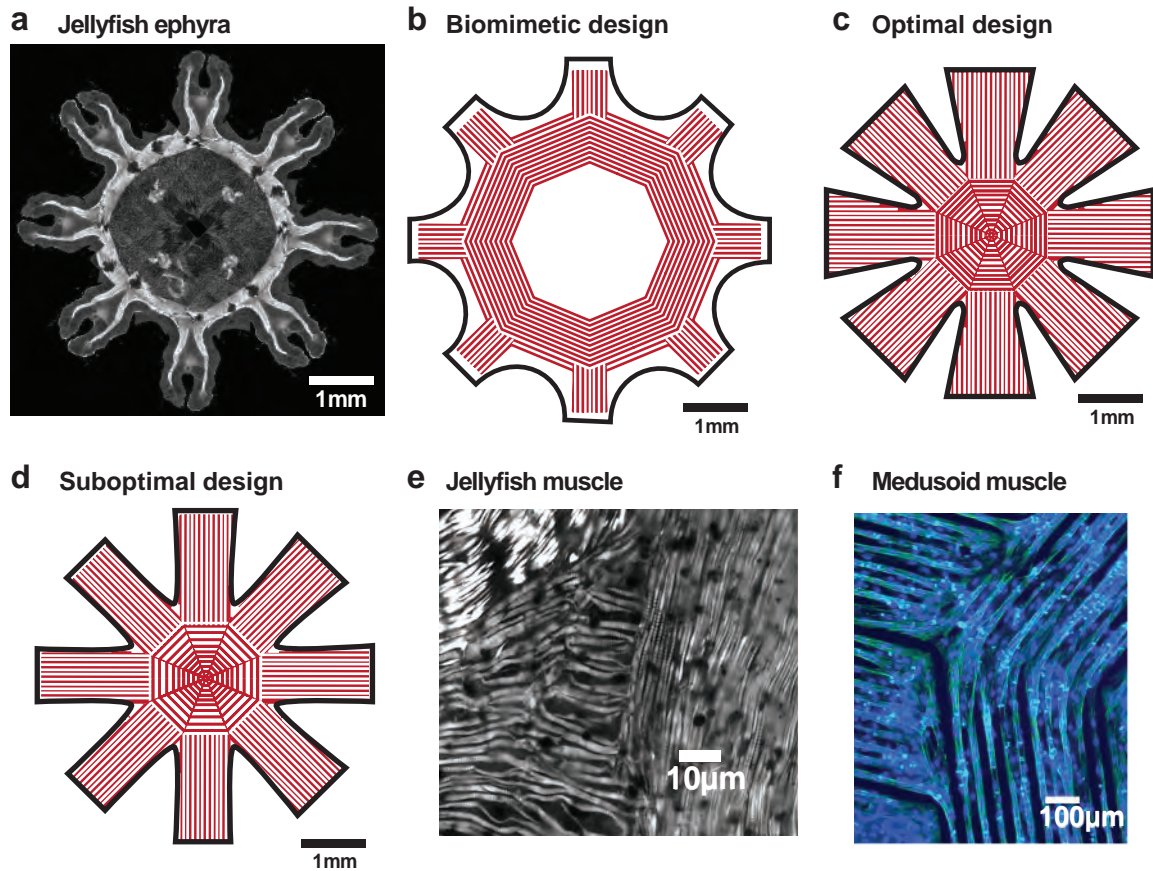


Supplementary Figures

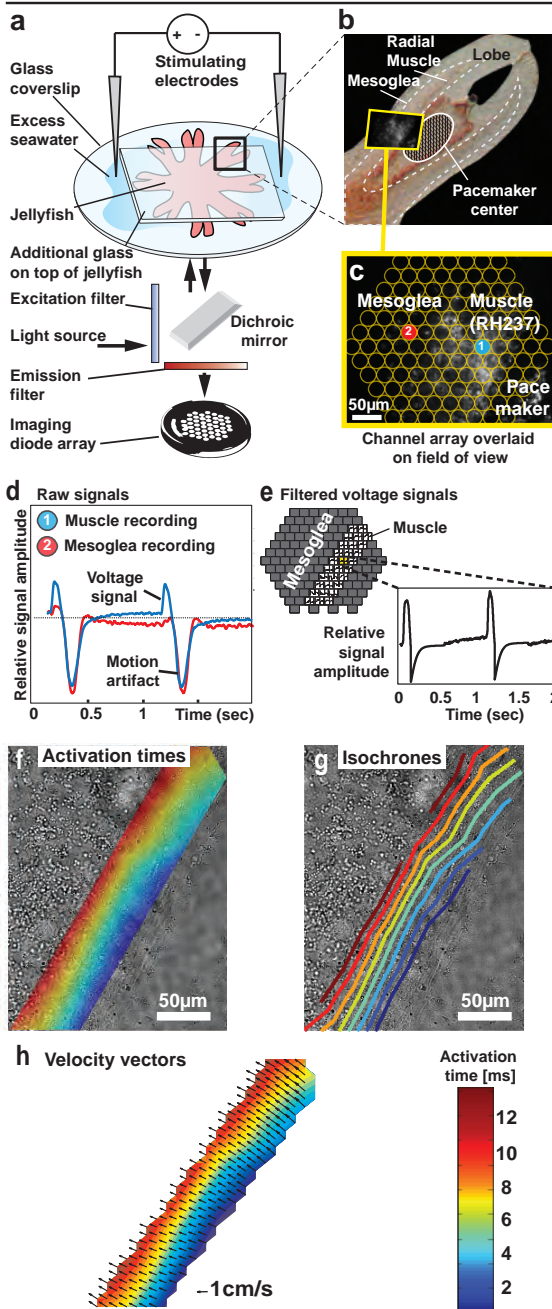


Supplementary Fig. 1 Engineering design algorithm for tissue-engineering functional constructs. The design algorithm consists of three phases - design, build and test. The series of steps is iterated until the engineered construct exhibits the desired functional performance. Design phase: Start by identifying quantitative benchmarks characterizing the desired function in a model system. Then, identify key design elements contributing to this function. Determine functionally equivalent bioengineered solutions from the pool of available materials. Build phase: Proceed by fabricating the bioengineered solution and standardize fabrication for repeatability. Test phase: Quantify implementation of key design elements including structural, physiological, kinematic and fluid dynamics characteristics. Finally compare functional performance to desired behavior using quantitative benchmarks. Return to design phase if performance is unsatisfactory.

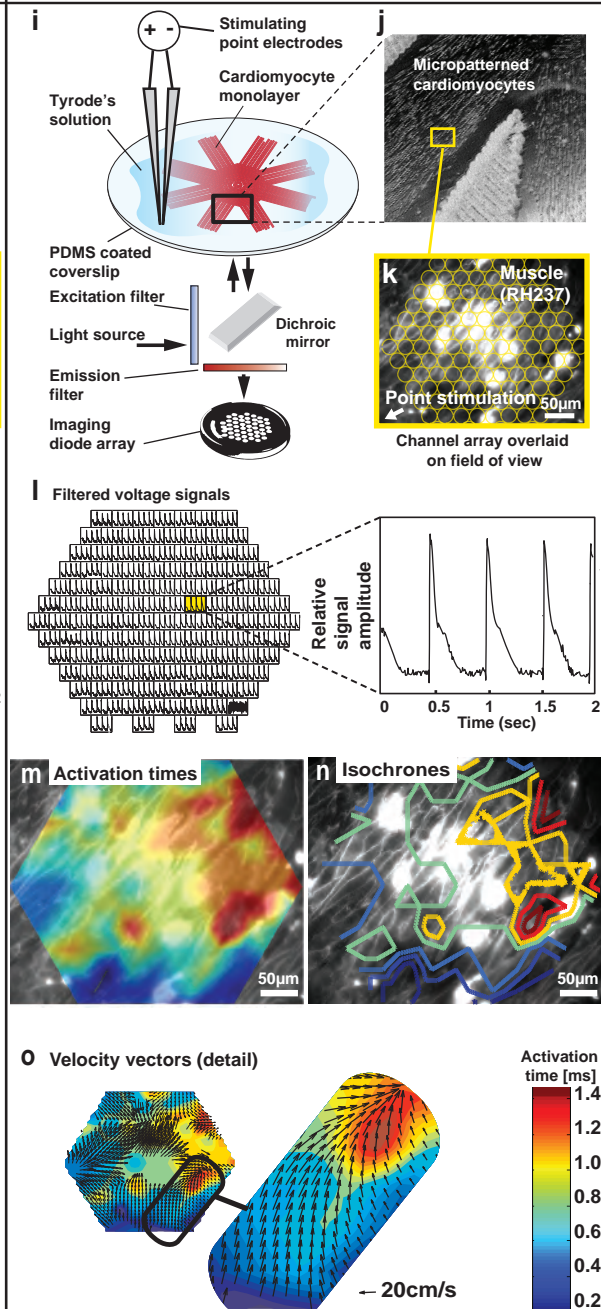


Supplementary Fig. 2 Jellyfish-inspired Medusoid muscle and body design. **a**, Muscle architecture in juvenile jellyfish showing radial and circular fiber orientations. Note: Composite image generated from single stained lobe copied and rotated to eight positions around central axis to extrapolate musculature of “entire” animal. White: F-actin stain. **b**, Biomimetic Medusoid muscle layout based on late-stage ephyrae. **c**, Final optimized Medusoid body and muscle layout with radial and circular fiber orientations. **d**, Suboptimal Medusoid design promoting inefficient fluid interactions (“sieve design”). **e**, Close-up on junction of radial and circular muscle in jellyfish. **f**, Close-up on junction of radial and circular muscle in Medusoid. Note: This tissue was micropatterned using 20 μm wide lines spaced by 20 μm to emphasize longitudinal edges and improve pattern visibility. Final constructs were patterned with 22 μm wide lines separated by 4 μm gaps resulting in confluent anisotropic tissue (Fig. 1f).

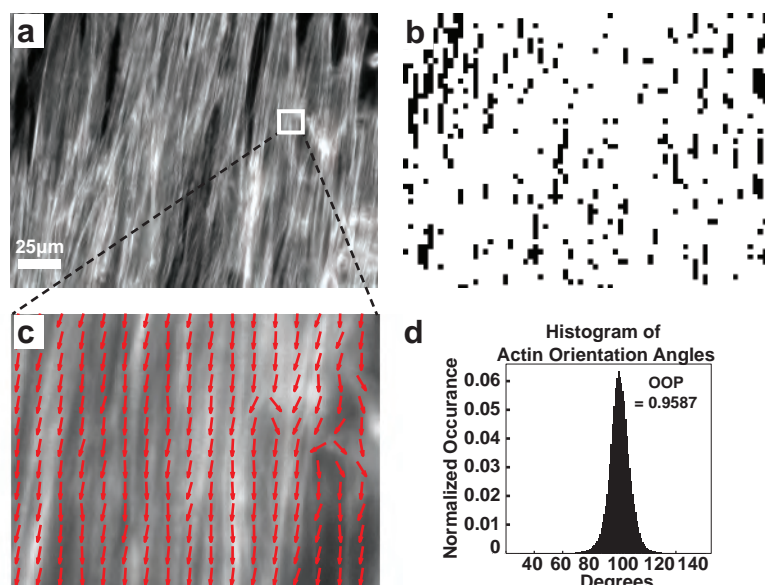
Jellyfish muscle physiology



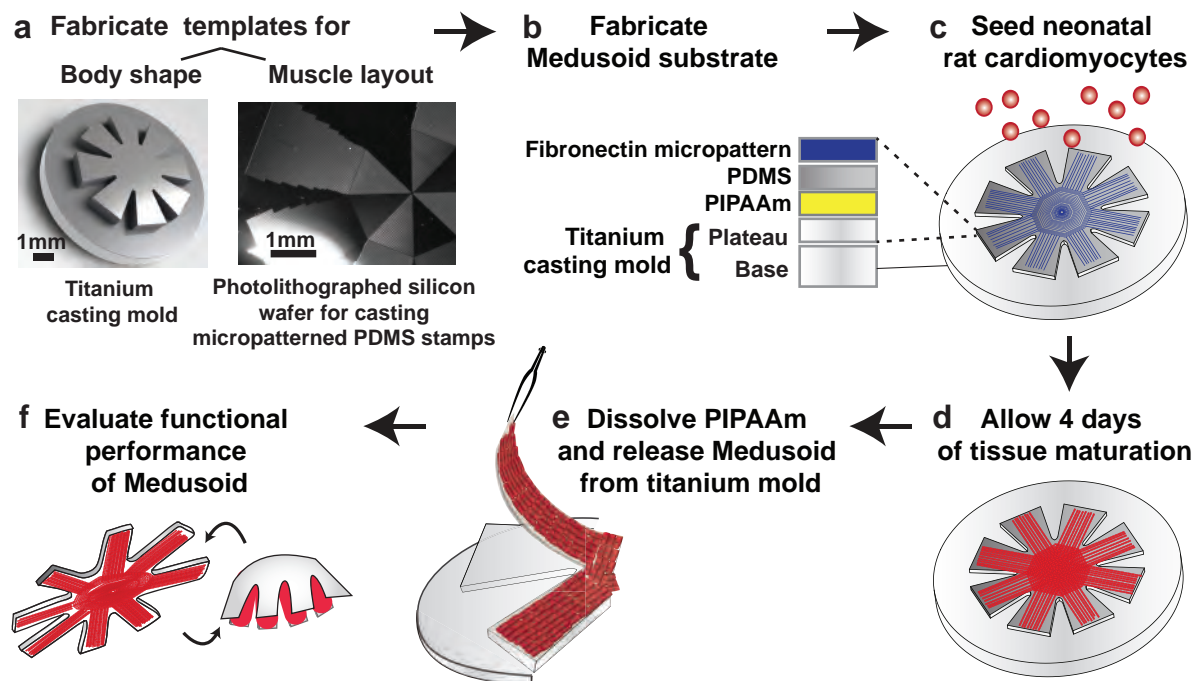
Medusoid muscle physiology



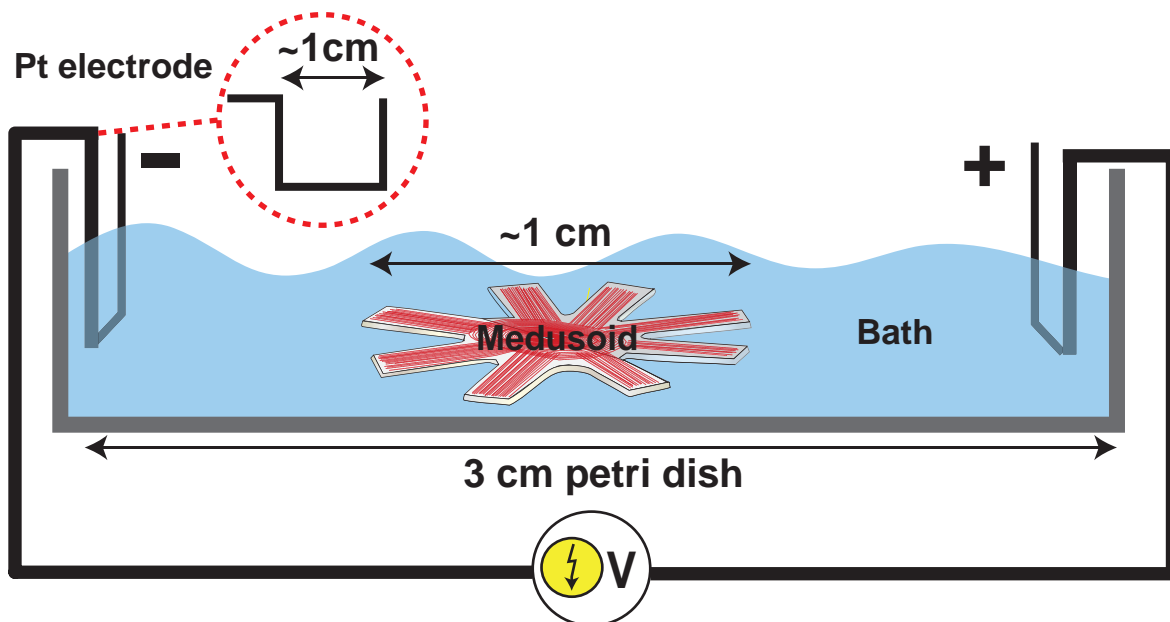
Supplementary Fig. 3 Optical mapping confirms continuous action potential propagation in Medusoid and Jellyfish striated muscle. **a**, Set-up of optical mapping system (OMS) for membrane voltage recording in jellyfish muscle stained with RH237. **b**, Close-up on jellyfish lobe with typical field of view (FOV) on RH237-stained radial muscle. **c**, FOV overlaid with LED recording array. The two labeled channels are representative for channels recording from muscle tissue (channel 1, blue) or from mesoglea (channel 2, red). **d**, Recording traces from the two channels marked in (c) illustrate that only muscle recordings contain voltage signals. **e**, Filtered data set only contains channels recording from muscle. **f-h**, Activation times and velocity vectors calculated from filtered data set in (e) illustrate spread of continuous wave front activating the jellyfish muscle. Mean conduction velocity: 1 ± 0.35 cm/s; $n=13$ FOVs (from 3 animals). **i**, OMS setup for membrane voltage recording in Medusoid muscle (anisotropic monolayer of cardiomyocytes). **j**, Close-up on Medusoid micropatterned muscle. **k**, Typical FOV of RH237-stained muscle tissue overlaid with LED recording array. **l**, Filtered voltage signal and exemplary trace recorded by single channel. **m-o**, Activation times and velocity vectors calculated from filtered data set in (l) illustrate spread of continuous wave front activating the Medusoid muscle. Mean conduction velocity: longitudinal, 27 ± 4 cm/s, transverse, 9 ± 1 cm/s; $n=4$ FOVs (from 2 Medusoid constructs).



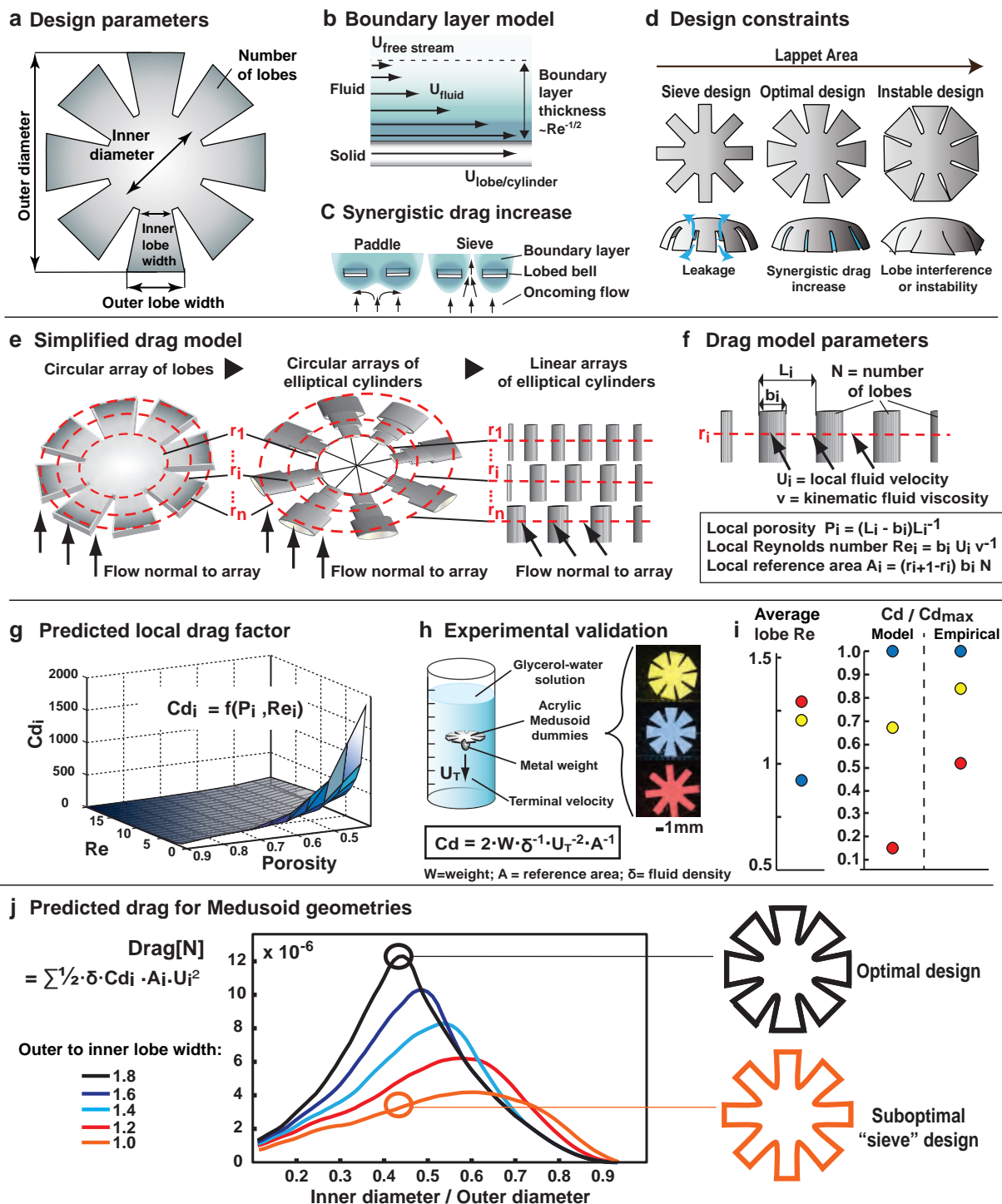
Supplementary Fig. 4 Processing steps of quantitative fiber alignment analysis. **a**, Original actin stain intensity image. **b**, Binary image mask with black regions indicating regions exempted from analysis. **c**, Detail of intensity image overlaid with local vector field showing tangential vector **d**, Histogram of all orientation vector angles, peaking at dominant fiber orientation. The corresponding orientational order parameter (OOP) is 0.9587.



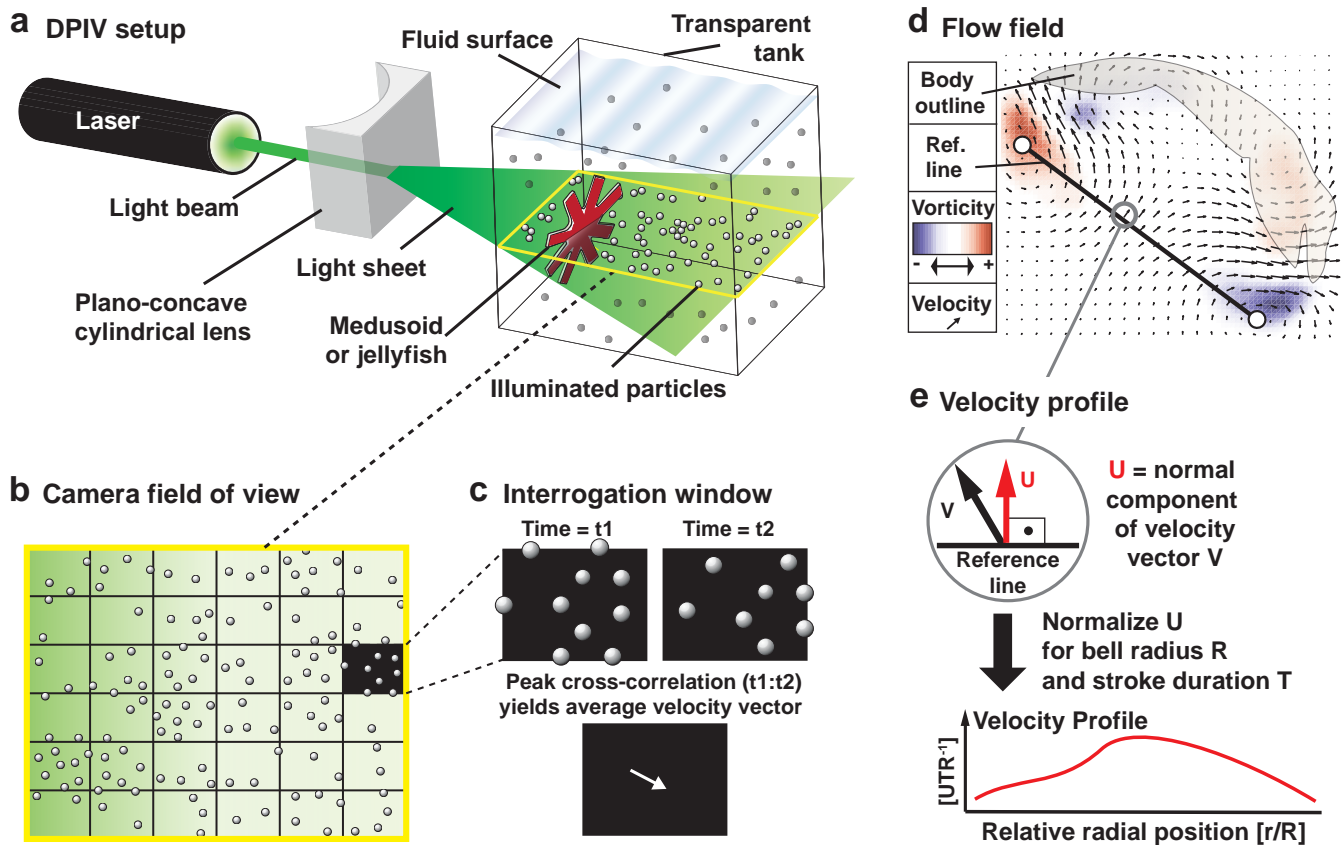
Supplementary Fig. 5 Medusoid fabrication process. **a**, Titanium casting molds and PDMS micropatterned stamps fabricated from photolithographed silicon wafers provided templates for Medusoid body shape and muscle layout, respectively. **b**, Medusoid substrates were fabricated by spin-coating the titanium casting mold with PIPAAm for temperature-sensitive adhesion to a PDMS top layer. Using PDMS stamps the PDMS layer was micropatterned with fibronectin to elicit cell adhesion and the formation of anisotropic Medusoid muscle tissue. **c**, Substrates were seeded with a suspension of freshly isolated neonatal rat cardiomyocytes. **d**, Medusoid substrates were cultured for four days to allow for maturation of the 2D myocardium. **e**, Lowering bath temperatures below 35°C dissolved the layer of PIPAAm, allowing to gently peel off the Medusoid from the titanium mold. **f**, The free-floating Medusoid was assayed for bell contraction and fluid transfer mimicking jellyfish feeding and swimming.



Supplementary Fig. 6 Experimental set-up for field stimulation of Medusoid constructs. An external field stimulator (Myopacer, IonOptix Corp.) generates monophasic square pulses (5–10 V, 10 ms duration, maximal current 65 mA) delivered to the bath (~10 ml Tyrode's solution at 37°C) by two U-shaped platinum electrodes flanking the construct. Pacing frequency ranged from 0.5 to 2 Hz.



Supplementary Fig. 7 Fluid-solid interaction and optimal Medusoid geometry. **a**, Medusoid geometric parameters. Free parameters: relative lobe length = inner to outer diameter, and lobe divergence = outer to inner lobe width. Fixed parameters: Outer diameter = 9 mm, number of lappets = 8. **b**, Viscous boundary layer model describing velocity gradient at solid-fluid interfaces. Thickness of boundary layer is proportional to $Re^{-1/2}$, with Re = local Reynolds number. **c**, Given suitable Medusoid geometry and flow conditions, overlap of neighboring boundary layers may occur, blocking interlobal gaps to oncoming flow. This raises both viscous and pressure drag, leading to synergistic increase in lobe drag and paddling efficiency (right) compared to the case of insufficient boundary layer overlap with interlobal leakage (left). **d**, Optimal Medusoid geometries (center) promote sufficient boundary layer overlap, thereby minimizing leakage through interlobal gaps (left), and avoid unstable or interfering lobe dimensions (right). **e**, Bell drag was estimated from simple fluid-solid interaction model. Medusoid lobes were represented as continuous arrays of elliptical cylinders perpendicular to flow. **f**, At each radial position, geometric and kinetic parameters are given from overall geometry and flow conditions, allowing to derive local porosity, Reynolds number and reference area. **g**, Local Reynolds number and porosity predict local drag coefficient. **h**, Empirical validation of the model was achieved by sinking acrylic Medusoid dummies of varying geometries in glycerol-water solutions. Drag factors were calculated from terminal sinking velocity. **i**, Empirical order of drag factors in Medusoid dummies was consistent with predicted order (right), and independent of the order of average lobe Reynolds numbers (left). Drag factors were normalized to respective maximal value. Color code relates dummy shapes depicted in (i) with plotted data. **j**, Total predicted drag as function of relative lobe length and divergence in live Medusoid tissue constructs. In general, higher lobe divergence resulted in higher maximal drag. For stability reasons lobe divergence did not exceed 1.8. Final optimal and suboptimal designs promoting paddling and sieving, respectively, are depicted to the left.



Supplementary Fig. 8 Digital particle image velocimetry (DPIV) setup and analysis. **a**, Basic DPIV set-up for jellyfish and Medusoids. A laser light beam is directed through a plano-concave cylindrical lens and thereby diverges into a light sheet of ca. 1 mm in thickness. This light sheet illuminates a plane within the particle-seeded fluid, thereby visualizing fluid motion in a single plane. **b**, Top-view onto plane of illuminated particles as seen by video camera. For flow analysis the field is divided into subsample areas, so-called interrogation windows. **c**, Each interrogation window is compared at time 1 (t_1) with the corresponding area at time 2 (t_2) in the following video frame. The average velocity vector for the window corresponds to the shift of particle positions at t_1 that results in matching most of the particle positions at t_2 , equal to peak cross-correlation between positions at t_1 and t_2 . **d**, The flow field is derived by plotting the average velocity vector for all windows in the field of view. Further analysis on the flow yields metrics such as vorticity (blue: clockwise; red: anti-clockwise) or the velocity profile across a line of reference (Ref. line). **e**, The non-dimensionalized velocity profile as a function of position is derived from the normal component of the velocity vectors across the line of reference. Here, the line of reference was chosen to be the diameter of the stopping vortex ring, allowing the characterization of flow towards the subumbrella at a certain instant during the recovery stroke (“feeding currents”).

Supplementary Movies

Supplementary Movie 1

This movie shows the stroke cycle in a free-swimming juvenile Moon jellyfish (*Aurelia aurita*) consisting of muscle-powered contraction (power stroke) and elastic recoil (recovery stroke).

Supplementary Movie 2

This movie shows the failure of a biomimetic Medusoid design to propel itself. The Medusoid construct was paced at 1 Hz through an externally applied monophasic square pulse (2.5V/cm, 10ms duration). Due to mismatch of muscle stresses and substrate compliance, muscle contraction does not result in sufficient bell deformation, and no thrust is generated.

Supplementary Movie 3

This movie demonstrates jellyfish-like body contraction and free-swimming of optimally designed Medusoid constructs. Medusoids were paced at 1 Hz through an externally applied monophasic square pulse (2.5V/cm, 10ms duration). The first scene shows a mature construct still attached at its center to its casting mold, just prior to release. (Note that the striated appearance of the casting mold is caused by its fabrication process; in particular, this striation does not reflect the alignment of the muscle tissue on top of the silicone membrane covering the mold). Subsequent scenes show exemplary propulsion of free-swimming Medusoids.

Supplementary Movie 4

This movie demonstrates comparative propulsion efficacy (distance per stroke) in jellyfish and optimal Medusoids, whereas suboptimal Medusoids (“sieve design”) exhibit inferior performance. While Medusoids were paced at 1 Hz through an externally applied electric field of 6 V, here the jellyfish contracts at a frequency of ca. 2 Hz. In order to facilitate comparison, the frame rate of the jellyfish recording was halved to synchronize stroke phases.

Supplementary Movie 5

This movie shows a sequence of raw DPIV data for jellyfish, Medusoid and suboptimally (=sieve-) designed Medusoids. Here, fluid flow around the jellyfish/Medusoid bell is visualized by the displacement of neutrally buoyant particles suspended within the fluid and illuminated within a single plane using laser light. The relative motion of the particles allows quantifying 2D fluid flow within the plane.

Supplementary Movie 6

This movie shows the fluid flow field and the vorticity field of a juvenile jellyfish during the stroke cycle. The movie was generated from DPIV data. The power stroke is characterized by maximal fluid velocities and formation of a starting vortex, generating thrust. The recovery stroke is characterized by reduced fluid velocities and the formation of a stopping vortex, generating feeding currents towards the subumbrellar side.

Supplementary Movie 7

This movie shows the fluid flow field and the vorticity field of an optimally designed Medusoid during the stroke cycle. The movie was generated from DPIV data. As in the jellyfish, the power stroke generates maximal fluid velocities and a starting vortex ring, resulting in thrust. The recovery stroke generates a stopping vortex ring that draws feeding currents towards the subumbrella.

Supplementary Movie 8

This movie shows the fluid flow field and the vorticity field of a suboptimal Medusoid design. The movie was generated from DPIV data. In contrast to jellyfish and optimal Medusoids, suboptimal Medusoids with “sieve design” fail to sufficiently accelerate fluid during the power stroke, resulting in poor thrust generation. Vorticity patterns are more diffuse compared to those observed in jellyfish and optimal designs, and further flow analysis revealed that generation of feeding currents was inferior as well (Fig. 4).